3-D cross-gradient joint inversion of seismic refraction and DC resistivity data

Zhanjie Shi[1,2,4] Richard W. Hobbs[2] Max Moorkamp[3] Gang Tian[4] Lu Jiang[1]

[1] *Institute of Culture and Heritage, Zhejiang University, Yuhangtang Road 866, Hangzhou 310058, China*

[2] *Department of Earth Sciences, Durham University, South Road, Durham DH1 3LE, UK*

[3] *Department of Geology, Leicester University, University Road, Leicester LE1 7RH,, UK*

[4] *School of Earth Sciences, Zhejiang University, Zheda Road 38, Hangzhou 310027, China*

Corresponding author: Zhanjie Shi, Email: shizhanjie@zju.edu.cn;

ABSTRACT

We present a 3-D cross-gradient joint inversion algorithm for seismic refraction and DC resistivity data. The structural similarity between seismic slowness and resistivity models is enforced by a cross-gradient term in the objective function that also includes misfit and regularization terms. A limited memory quasi-Newton approach is used to perform the optimization of the objective function. To validate the proposed methodology and its implementation, tests were performed on a typical archaeological geophysical synthetic model. The results show that the inversion model and physical parameters estimated by our joint inversion method are more consistent with the true model than those from single inversion algorithm. Moreover, our approach appears to be more robust in conditions of noise. Finally, the 3-D cross-gradient joint inversion algorithm was applied to the field data from Lin_an ancient city site in Hangzhou of China. The 3-D cross-gradient joint inversion models are consistent with the archaeological excavation results of the ancient city wall remains. However, by single inversion, seismic slowness model does not show the anomaly of city wall remains and resistivity model does not fit well with the archaeological excavation results. Through these comparisons, we conclude that the proposed algorithm can be used to jointly invert 3-D seismic refraction and DC resistivity data to reduce the uncertainty brought by single inversion scheme.

Keywords: seismic refraction; DC resistivity; 3-D joint inversion; cross-gradient structural constraint;

1 Introduction

Collated seismic refraction and DC resistivity has become a popular method because the combined usage of both methods can decrease the ambiguity inherent to the individual use of the methods in near surface investigation (Hellman et al. 2012). Compared with separate inversion schemes for each method leading sometimes to models that are not in good accord, joint inversion of seismic refraction and DC resistivity data can provide a better interpreted model (Gallardo and Meju, 2004). However, simultaneous invertion of seismic refraction and DC resistivity data using 3-D joint inversion scheme has not been developed.

Joint inversion schemes that have been successfully applied to various kinds of geophysical data (e.g., Benech et al., 2002; Linde et al., 2008; Fregoso and Gallardo, 2009; Vermeesch et al.,

2009; Doetsch et al., 2010, 2012; Bouchedda et al., 2012; Orlando, 2013). For joint inversion of geophysical data that are sensitive to different physical parameters, such as seismic velocity and resistivity, a relationship between different physical parameters needs to be formulated to couple the two or more inversion models. Generally speaking, two approaches, direct parameter relationship and structural constraint are used in linking the different physical parameters in joint inversion (Moorkamp et al., 2013).

For the direct parameter relationship, we need specify a functional relation between different parameters. Such functional relation can be deduced from an empirical formula (De Stefano et al., 2011) or derived from various logging data (Heincke et al., 2006; Jegen et al., 2009). The direct parameter relationships provide a strong coupling between the data sets. Though good joint inversion results can be obtained from direct parameter coupling approach it can result in spurious features when the models violate the parameter relationships (Moorkamp et al., 2011). It is difficult to derive an appropriate function relation between seismic velocity and resistivity due to the complication of the near surface heterogeneity, so it is unlikely that we would obtain useful results from joint inversion of seismic refraction and DC resistivity data using direct parameter relation approach.

Structural constraint approaches don't need a functional relation between different physical parameters and couple two or more inversion models by measuring the structural similarity between them (Zhang et al., 1997; Haber et al., 1997; Gallardo et al., 2003; Günther et al., 2006). For example, the cross-gradient scheme evaluates the structural features common to different geophysical methods by specifying a cross-gradient function incorporated as a constraint in a nonlinear least squares problem formulation (Gallardo et al., 2004). 2-D joint inversion of seismic refraction and DC resistivity with cross-gradient constraint has been successfully applied in the characterization of near surface heterogeneous materials (Gallardo and Meju, 2003, 2004; Infante et al., 2010; Hamdan and Vafidis, 2013). However, 3-D joint inversion of seismic refraction and DC resistivity data has not been previously tried though 3-D scheme should give more accurate results for 3-D geophysical structures. Also there is an increasing need for a 3-D joint inversion schemes for 3-D seismic refraction and DC resistivity surveys that are becoming more common in near surface investigation (Leucci et al., 2007; Heincke et al., 2010; Shahrukh et al., 2012; Loke et al. 2013).

In this paper, we developed a 3-D cross-gradient joint inversion algorithm of seismic refraction and DC resistivity data based on the framework for 3-D joint inversion (Moorkamp et al., 2011). First, we present the method and algorithm of 3-D cross-gradient joint inversion of seismic refraction and DC resistivity data. Then we use a synthetic example to describe the pertinent details of implementation and compare joint inversion models with individual inversion results. Finally the scheme is applied to field data from an archaeological site in the southeast of China to further demonstrate the effectiveness of the joint inversion procedure.

2 Joint inversion method

The objective function of 3D cross-gradient joint inversion includes three parts that are misfit function, model regularization function and cross-gradient term. Moorkamp et al. (2011) have described the objective function definition in detail. So here we only briefly present the definition and mainly discuss the specifics that relate to 3D joint inversion of seismic refraction and DC

resistivity data.

The definition of misfit objective function ϕ_d follows the approach of Tarantola (2004),

$$\phi_d(m) = [f(m) - d_{obs}]^T C_d^{-1}[f(m) - d_{obs}],$$ (1)

where m is the model parameters, $f(m)$ is the synthetic data and d_{obs} is the observed data. For seismic refraction, m and $f(m)$ (or d_{obs}) correspond to the slowness $s(s/m)$ and travel time. For DC resistivity, m and $f(m)$ (or d_{obs}) correspond to the resistivity $\rho(ohm.m)$ and projected potential or apparent resistivity. C_d^{-1} is the inverse of the observed data covariance matrix that reduces the influence of observations with large errors.

The regularization objective function ϕ_{reg} is defined as,

$$\phi_{reg}(m) = \sum_i \alpha_i(m - m_0)^T W_i^T C_M^{-1} W_i(m - m_0) + \beta(m - m_0)^T C_M^{-1}(m - m_0),$$ (2)

where: the three axes directions $i = \{x, y, z\}$ are summed; α_i are weight factors used to weight the contribution for each direction; m_0 is an a priori model that is commonly equal to the average value of slowness and resistivity of the survey area for seismic refraction and DC resistivity respectively; W_i are finite difference approximations to the first or second spatial derivative of the model parameters in the respective direction (Farquharson and Oldenburg, 1998), W_i can be used to seek a model that has a minimum parameter variation between adjacent cells or minimum curvature; and C_M is a model covariance matrix. The second term in Eq.(2) is used to minimize the total value of the model vector and the weight β is usually kept as a small value.

The cross-gradient function, ϕ_{cross}, of seismic refraction and DC resistivity is introduced by Gallardo and Meju (2003) and has the form,

$$\phi_{cross}(m) = (\nabla m_1 \times \nabla m_2)^T C_M^{-1}(\nabla m_1 \times \nabla m_2),$$ (3)

where m_1 and m_2 are the parts of the model vector m that correspond to slowness and resistivity respectively.

We sum the above three objective functions and obtain the joint inversion objective function of seismic refraction and DC resistivity as follows,

$$\phi_{joint} = \phi_{d,seis} + \phi_{d,dc} + \phi_{reg,s} + \phi_{reg,\rho} + \phi_{cross,s/\rho},$$ (4)

where the indices $d, seis$, d, dc represent the misfit for the seismic refraction and DC resistivity data, respectively; reg, s, reg, ρ denote the regularization term for the slowness and resistivity section of the model vector respectively; and $cross, s/\rho$ denotes the cross-gradient term between slowness and resistivity sections of model vector. Within the objective function in Eq.(4), we can adjust the relative weighting for the different terms by dividing the respective covariances by a factor α (Moorkamp et al., 2011).

The optimization of the objective function is performed using a limited memory quasi-Newton approach (L-BFGS) (Avdeev and Avdeeva, 2009). For 3-D joint inversion of seismic refraction and DC resistivity data, given a starting model m_0, a number of optimization iterations are performed until the value of the objective function ϕ, the misfit between observed and synthetic data, reaches a certain threshold. At each iteration, after the calculation of the misfit and the gradient of the objective function for the current model, we use L-BFGS to transform the gradient to a search direction p_i and calculate an optimum step length μ using the line search procedure of Moré and Thuente (1994) to update the current model,

$$m_{i+1} = m_i + \mu p_i,$$ (5)

3 Joint inversion algorithm

Fig.1 is the flowchart for the 3-D cross-gradient joint inversion of seismic refraction and DC resistivity data. The core inversion algorithm only perturbs the vector according to the objective function and gradient values with no regard to the meaning of the inversion parameters m. But the forward modeling, the calculation of objective functions for seismic refraction and DC resistivity method expect the natural physical parameters slowness s and resistivity ρ, respectively. So we use a transformation function "Para trans." module shown in Fig. 1 to translate between the generalized model parameters and the physical parameters. As is shown in Fig. 1, we first give a starting model and calculate joint objective function. Then perform a number of optimization iterations until the value of the objective function, the misfit between observed and forward data, reaches a certain threshold. Finally joint inversion results corresponding to seismic refraction and DC resistivity method are output separately. We describe main parts of the flow shown in Fig.1 in detail below.

2.1 Forward modeling

Finite difference computation of seismic travel time is based on the code of Podvin and Lecomte (1991). The code can simulate the propagation of wavefronts in arbitrary velocity models using a parallel method. For the DC resistivity modeling, finite volume approach is used to calculate electrical potential based on the Matlab code of Pidlisecky et al. (2007). We further develop the code to calculate apparent resistivity to meet the requirement that the DC resistivity field data are normally collected in the form of apparent resistivity.

The forward modeling algorithms of seismic refraction and DC resistivity data have different mesh requirements though they both adopt rectilinear meshes. The travel time code requires that

all grids have the same size in all three directions. For DC resistivity, finite volume approach is used to discretize the system and the meshes generated are more flexible. Commonly, in order to keep consistent with variation of electrical potential, the parts of model near the source electrodes are discretized using denser grids and the parts of model far away from the source electrodes are discretized using coarser grids. So we separate the inversion meshes from the forward meshes and use a simple form of model refinement where for the forward modeling new cell boundaries can be added to the inversion meshes and the exiting boundaries of the inversion grids are preserved. Thus, the different refinement grids can meet the requirements for forward modeling of both seismic refraction and DC resistivity data.

2.2 Model parameterization

The core inversion algorithm operates on a vector of generalized model parameters m . The forward modeling and the calculation of objective function for both methods use the physical parameters slowness s and resistivity ρ . Two transformation function $s(m)$, $\rho(m)$ are defined to translate between the generalized model parameters and physical parameters.

For seismic method, the form of the transformation function is as follows,

$$s_{i(m_{s,i})} = s_{\min} + \frac{1 + \tanh(m_{s,i})}{2}(s_{\max} - s_{\min}),$$

(6)

where, the smallest slowness $s_{\min}$ and the biggest slowness $s_{\max}$ are used to guarantee that each element of m varies throughout the whole numerical range while the corresponding slowness values are restricted between $s_{\min}$ and $s_{\max}$ (Commer and Newman, 2008).

The definition of transformation function $\rho(m)$ is similar with $s(m)$. Because the logarithm of resistivity is used to reduce the influence of the large magnitude of resistivity value, $\rho(m)$ has a form,

$$\log(\rho_j(m_{\rho,j})) = \log(\rho_{\min}) + \frac{1 + \tanh(m_{\rho,j})}{2}(\log(\rho_{\max}) - \log(\rho_{\min})),$$

(7)

where $\rho_{\min}$, $\rho_{\max}$ are the smallest and the biggest resistivity respectively. When running the joint inversion code, the generalized model vector m contains two segments, m_s and m_ρ, that correspond to slowness and resistivity.

2.3 Gradient calculation

The optimization algorithm L-BFGS requires the gradient of the objective function with respect to the generalized model parameters. If the DC resistivity forward modeling data is $p = \varphi(m)$ in Eq.(1), given all the steps described above and we can write $\varphi(m)$ as,

$$\varphi(m) = \varphi\{III[\rho(m)]\},$$

(8)

where III represents the model refinement function that transforms the inversion grids Ψ shown in Fig. 1 to the new grids used in forward modeling.

The gradient of objective function is calculated using the chain rule and has the following form,

$$\frac{\partial \phi_{dc}}{\partial m_\rho} = \frac{\partial \rho}{\partial m_\rho} \frac{\partial III}{\partial \rho} \frac{\partial \varphi}{\partial III} \frac{\partial \phi_{dc}}{\partial \varphi}, \tag{9}$$

where $\frac{\partial \varphi}{\partial III}$ is the sensitivity matrix for the DC resistivity data with respect to the refined grid. Since the sensitivity matrix for the DC resistivity data is a very large, dense matrix (Haber et al., 2000), we calculate it only by computation the product of three sparse matrixes using a J algorithm that J is the sensitivity matrix and can be calculated through a series of matrix-vector products (Pidlisecky et al., 2007). The term $\frac{\partial \rho}{\partial m_\rho}$ relates the changes of the objective function with respect to the physical parameters to the generalized model parameters. And the term $\frac{\partial III}{\partial \rho}$ describes how the refined grid changes the resistivity parameter.

For seismic refraction method, the calculation of gradient of objective function has been discussed by Moorkamp et al. (2011) in detail. So we don't discuss them here. Once the gradient for the both type of data, regularization and cross-gradient terms have been calculated, we can obtain the gradient of joint inversion objective function by summing all separate gradients,

$$\frac{\phi_{jo\,int}(m)}{\partial m} = \frac{\phi_{d,seis}(m)}{\partial m} + \frac{\phi_{d,dc}(m)}{\partial m} + \frac{\phi_{cross,s/\rho}}{\partial m} + \frac{\phi_{reg,seis}}{\partial m} + \frac{\phi_{reg,dc}}{\partial m}, \tag{10}$$

Then we can use this gradient to update the inversion model using the optimization algorithm, L-BFGS.

4 Synthetic example

To evaluate the validity of the 3-D joint inversion approach on seismic refraction and DC resistivity data, we first performed a test on a synthetic model (Fig. 2). In our experiment, the goal is to image the archaeological remains buried in near surface layers, such as the ancient wall and paleo-channel which are common in archaeological prospection (Shi et al., 2015). The model consists of $20 \times 20 \times 10$ cubic cells with the same edge length of 1 m. Two rectangular anomalies spaced 2 m apart are generated and have the same length of 10 m, width of 2 m, thickness of 2 m and burial depth of 2 m (Fig. 2). As is shown in Fig. 3, the two anomalies have the same seismic velocity of 2000 m.s^{-1} while have the resistivity values of 10 ohm.m, 300 ohm.m, respectively. We designed a layered background with seismic velocity linearly increasing from the surface layer of 500 m.s^{-1} to the bottom layer of 800 m.s^{-1} and with resistivity values linearly decreased from the surface layer of 30 ohm.m to the bottom layer of 20 ohm.m.

From the above models we calculated synthetic traveltimes and apparent resistivity data using the finite difference code (Podvin and Lecomte, 1991) and the finite volume approach (Pidlisecky et al., 2007), respectively. The distribution of seismic sources, receivers and DC resistivity electrodes are shown in Fig. 2. On the surface, 100 seismic sources were located with the distance separated by 2 m and 324 receivers were spaced at 1 m on the regular grids. For all 32400

source-receiver combinations, we calculated synthetic traveltimes. For DC resistivity data, we placed 96 electrodes on the surface. Of the 96 electrodes, we used 58 electrodes as both current electrodes and potential electrodes while the remaining 38 as potential electrodes only. There were 41 independent current pairs. For each current pair, data were calculated for the remaining 94 electrodes using dipole-dipole resulting in 93 independent data points. So we acquired a total of 3813 data points for the entire survey. These data, without noise, were used as the observed data for 3-D joint inversion experiment.

Starting from two models that are the layered background without the two anomalies, we performed the individual inversion and 3-D cross-gradient joint inversion for seismic refraction and DC resistivity data. For a single seismic tomographic inversion and DC resistivity inversion, the weight for the covariance scaling factors of regularization terms are $\alpha_{reg,s}$ =100 and $\alpha_{reg,\rho}$ =50, respectively. We constrained the slowness between 0.000333 and 0.005 s.m^{-1}, corresponding to the velocities of 3000 and 200 m.s^{-1}, respectively. The resistivity was restricted between 5 ohm.m and 600 ohm.m. For 3-D cross-gradient joint inversion, we used the same weight for regulation terms and the same physical parameter ranges. In addition, we run the 3D cross-gradient joint inversion by setting the weight $\alpha_{cross,s/\rho}$ =10^6 for the cross-gradient term.

Fig. 4 shows the results of the individual inversion and 3-D cross-gradient joint inversion for seismic refraction synthetic data without noise. The horizontal slices at the depth of 3 m and the vertical depth slices through the model center for individual inversion are shown in Fig. 4a and Fig. 4c, respectively. We observe that the shape recovered by individual seismic tomographic inversion has some small difference with the true model. We also see the transition between the two anomalies is blurred and around the two anomalies we observe some artifacts in the background. The horizontal slice at the depth of 3 m and the vertical depth slices through the model center for 3D joint inversion are shown in Fig. 4b and Fig. 4d. We can see some minor improvement over the individual inversions in Fig. 4b and Fig. 4d. The shape and position of the two anomalies recovered by joint inversion are more close to the true model. And the artifacts in the background are reduced in joint inversion images. To improve the visibility of fluctuation from the true model, we plot relative difference shown in Fig. 5 between the seismic inversion results and the true model. Horizontal slice at the depth of 3m and vertical depth slice through the model center of relative difference between single inversion result and the true model are shown in Fig. 5a and Fig. 5c, respectively. Fig. 5b and Fig. 5d are the horizontal slice and vertical depth slice images of relative difference between joint inversion result and the true model. From Fig. 5, we can see single inversion shows larger deviations from the true model than that from joint inversion. This indicates the precision of joint inversion model is higher than that from single inversion.

Fig. 6 shows the results of the individual inversion and 3-D cross-gradient joint inversion for DC resistivity synthetic data without noise. The horizontal slices of inversion model from individual inversion and 3-D joint inversion are shown in Fig. 6a and Fig. 6b, respectively. Compared the individual inversion, 3-D joint inversion improves the shape of anomalies. Fig. 6c and Fig. 6d show the vertical depth slices through model center of individual inversion and 3-D joint inversion, respectively. We observe the shape and position of the two anomalies recovered by 3-D joint inversion are more consistent with the true model. Fig. 7 shows the relative difference

between the resistivity inversion models and the true model. From Fig. 7, we observe that for most of the area, the relative difference of joint inversion result is less than that from single inversion.

In order to test the effect of noise on inversion results, in the second experiment, a standard deviation of 0.6 ms Gaussian noise was added to the synthetic traveltimes of the seismic model and 2 percent Gaussian noise was added to the DC resistivity data. The inversion parameters and flow are the same with those corresponding to the synthetic data without noise. Fig. 8 and Fig. 10 show that the seismic inversion results and resistivity inversion models, respectively. The relative difference results of seismic inversion and resistivity inversion models are shown in Fig. 9 and Fig. 11, respectively. From Fig. 4 and Fig. 8, we can see that the inversion models from the seismic synthetic data without noise are more consistent with the true models than those from the synthetic data with noise. However, after adding noise to synthetic data, the single inversion model shows more obvious inconsistencies with the true model. The joint inversion of the synthetic data with noise still successfully recovers the shape and position of anomaly. From Fig. 6 and Fig. 10, we observe that, after adding noise, single inversion does not reconstruct the shape and position of high resistivity anomaly whereas those of joint inversion model are consistent with the true model. From Fig. 5 and Fig. 9, we can see that the relative differences of inversion models are increased after adding noise to synthetic data. The relative difference increment of single inversion model is much more than that of joint inversion model. From Fig. 7 and Fig. 11, we also can observe the similar phenomenon. The above comparison shows that the joint inversion approach has higher robustness in the conditions of noise.

5 Field example

5.1 Field site description and data acquisition

The field data was collected from Lin_an ancient city site which lies in the main urban area of Hangzhou, southeast of China (Fig. 12). Lin_an city was constructed in the A.D. 1129 and now has been almost completely erased by human activities. Experiment was performed in an area where buried city wall remains have been occasionally found during the construction of building foundations. Before archaeological excavation of the wall remains, 3D seismic refraction and DC resistivity survey was acquired. The survey lines are in a 3D survey area shown in Fig. 12 and perpendicular to the expected trend of wall remains.

Fig. 13 shows the distribution of seismic sources, receivers and DC resistivity electrodes. On the surface we placed 60 geophones along five receiver lines with a transverse distance of 1.5 m and 12 receivers were deployed along each line with a trace distance of 1 m. 36 source points were located along the four source lines with a transverse distance of 1.5m in the middle of receiver lines and 9 shots were deployed along each line with a distance of 2 m. Additional 6 source points were placed at the ends of the two boundary receiver lines. The data were recorded by a SE2404NT seismograph using geophones with a natural frequency 100Hz. We acquired seismic refraction data from 2520 source-receiver combinations. The DC resistivity data were collected from 112 electrodes along seven survey lines with a transverse distance of 1 m and 16 electrodes were deployed along each line with a trace distance of 1 m. An E60 DC Resistivity Instrument was used to acquire 2245 data point in the form of dipole-dipole.

5.2 Individual inversion results

We first performed the individual inversion of seismic refraction and DC resistivity field data using an initial layered model with seismic velocity linearly increasing from the surface layer of 800 m.s^{-1} to the bottom layer of 1200 m.s^{-1} and with resistivity values linearly decreased from the surface layer of 30 ohm.m to the bottom layer of 20 ohm.m. The model consists of 36 $\times$ 16 $\times$ 12 cubic cells with the same edge length of 0.5 m. We constrained the slowness between 0.0004 and 0.01 s/m that correspond to velocities of 2500 and 100 m/s. The resistivity search range is from 0.1 to 2000 ohm.m. And we chose the values for the covariance scaling factors of regularization terms are $\alpha_{reg,s} =100$ and $\alpha_{reg,\rho} =100$ after testing over a range of values.

Fig. 14 shows the results of individual inversion from seismic refraction and DC resistivity field data. Fig. 14a and Fig. 14b show horizontal slices at the depth of 3.5m for seismic slowness and resistivity models, respectively. And the vertical depth slices through the model center for seismic slowness and resistivity are shown in Fig. 14c and Fig. 14d, respectively. The aerial photography of archaeological excavation result of wall remains is shown in Fig. 12. The archaeological excavation result shows that the wall remains consist of bricks and stones. The width of the wall remains is about 6 m and buried depth of the top is about 2 m. From Fig. 14, we observe that the shape and position of wall remains cannot be recovered by seismic inversion. The resistivity inversion successfully identifies the anomaly caused by the wall remains but the lower right parts are not well recovered.

5.3 Joint inversion results

Using the same initial model parameters, we performed the 3-D cross-gradient joint inversion of seismic refraction and DC resistivity field data. In the joint inversion experiment, the values for the covariance scaling factors of regularization terms are $\alpha_{reg,s} =100$ and $\alpha_{reg,\rho} =100$ and the weight for the cross-gradient term $\alpha_{cross,s/\rho} =10^3$.

The joint inversion results from seismic refraction and DC resistivity field data are shown in Fig. 15. Fig. 15a and Fig. 15b show horizontal slices at the depth of 3.5m for seismic slowness and resistivity models, respectively. The vertical depth slices through the model center for seismic slowness and resistivity are shown in Fig. 15c and Fig. 15d, respectively. From Fig. 15, we can see that the high resistivity anomaly is consistent with the wall remains both in terms of the shape and position. Also, we observe that joint inversion improves seismic model to a significant extent and seismic slowness model now shows the location of the object. The comparison between single inversion and joint inversion results indicates that the 3-D joint inversion approach is better than single inversion scheme.

6 Conclusion

3-D cross-gradient joint inversion algorithm is presented and a test of the proposed approach has been undertaken using synthetic and field data. In comparison to single inversion, experiments

using synthetic data demonstrate that the proposed algorithm improves accuracy of the models and precision of estimated physical parameters. Moreover, the 3-D joint inversion approach is more robust in conditions of noise. The comparison between single inversion and joint inversion results in the field example further proves the validity of the new algorithm. We conclude that the proposed approach is effective for joint inversion of 3-D seismic refraction and DC resistivity data.

Acknowledgement

References

Avdeev, D., Avdeeva, A., 2009. 3D magnetotelluric inversion using a limited-memory quasi-Newton optimization. Geophysics 74, F45-F57.

Benech, C., Tabbagh, A., Desvignes, G., 2002. Joint inversion of EM and magnetic data for near-surface studies. Geophysics 67, 1729-1739.

Bouchedda, A., Chouteau, M., Binley, A., Giroux, B., 2012. 2-D joint structural inversion of cross-hole electrical resistance and ground penetrating radar data. Journal of Applied Geophysics 78, 52-67.

Commer, M., Nweman, G.A., 2008. New advances in three-dimensional controlled-source electromagnetic inversion. Geophysical Journal International 172, 513-535.

De Stefano, M., Andreasi, F.G., Re, S., Virgilio, M., Snyder F.F., 2011. Multiple-domain, simultaneous joint inversion of geophysical data with application to subsalt imaging. Geophysics 76, R69-R80.

Doetsch, J., Linde, N., Coscia, I., Greenhagh S.A., Green A.G., 2010. Zonation for 3D aquifer characterization based on joint inversion of multimethod crosshole geophysical data. Geophysics 75, G53-G64.

Doetsch, J., Linde N., Pessognelli, M., Green A.G., Günther T., 2012. Constraining 3-D electrical resistance tomography with GPR reflection data for improved aquifer characterization. Journal of Applied Geophysics 78, 68-76.

Farquharson, C.G., Oldenburg, D.W., 1998. Non-linear inversion using general measures of data misfit and model structure. Geophysical Journal International 134, 213-227.

Fregoso, E., Gallardo, L.A., 2009. Cross-gradients joint 3D inversion with applications to gravity and magnetic data. Geophysics 74, L31-L42.

Gallardo, L.A., Meju, M.A., 2003. Characterization of heterogeneous near-surface materials by joint 2-D inversion of dc resistivity and seismic data. Geophysical Research Letters 30, 1658-1661.

Gallardo, L.A., Meju, M.A., 2004. Joint two-dimensional DC resistivity and seismic travel time inversion with cross-gradients constrains. Journal of Geophysical Research 109, B03311-B03321.

Günther, T., Bentley L.R., Hirsch M., 2006. A new joint inversion algorithm applied to the interpretation of DC resistivity and refraction data. SAGEEP, Seattle (USA).

Haber, E., Oldenburg D., 1997. Joint inversion: a structural approach. Inverse Problems 13, 63-77.

Haber, E., Ascher, U.M., Oldenburg, D., 2000. On optimization techniques for solving nonlinear inverse problems. Inverse Problems 16, 1263-1280.

Hamdan, H.A., Vafidis, A., 2013. Joint inversion of 2D resistivity and seismic travel time data to image salowater intrusion over karstic areas. Environment Earth Science 68, 1877-1885.

Heincke, B., Jegen, M., Hobbs, R., 2006. Joint inversion of MT, Gravity and Seismic Data applied to sub-besalt imaging. SEG Tech. Prog. Expand. Abstracts 25, 784-789.

Heincke, B., Günther, T., Dalsegg, E., Rønning J.S., Ganerd, G.V., Elvebakk, H., 2010. Combined three-dimensional electric and seismic tomography study on the Åknes rockslide in western Norway. Journal of Applied Geophysics 70, 292-306.

Hellman, K., Günther, T., Dahlin, T., 2012. Application of joint inversion and fuzzy C-means cluster analysis for road pre-investigations. EMEEG, Paris (Frace).

Infante, V., Gallardo, L.A., Montalvo-Arrieta, J.C., de León, I.N., 2010. Lithological classification assisted by the joint inversion of electrical and seismic data at a control site in northeast Mexico. Journal of Applied Geophysics 70, 93-102.

Jegen, M.D., Hobbs, R.W., Tarits, P., Chave, A., 2009. Joint inversion of marine magnetotelluric and gravity data incorporating seismic constraints. Earth and Planetary Science Letters 282, 47-55.

Leucci, G. Greco, F., De Giorgi, L., Mauceri, R., 2007. Three-dimensional image of seismic refraction tomography and electrical resistivity tomography survey in the castle of Occhiolà (Sicily, Italy). Journal of Archaeological Science 34, 233-242.

Linde, N., Tryggvason, A., Peterson, J.E., Hubbard, S.S., 2008. Joint inversion of crosshole radar and seismic traveltimes acquired at the South Oyster Bacterial Transport Site. Geophysics 73, G29-G37.

Loke, M.H., Chambers, J.E., Rucker, D.F., Kuras, O., Wilkinson, P.B., 2013. Recent developments in the direct-current geoelectrical imaging method. Journal of Applied Geophysics 95, 135-156.

Moorkamp, M., Heincke, B., Jegen, M., Roberts, A.W., Hobbs, R.W., 2011. A framework for 3-D joint inversion of MT, gravity and seismic refraction data. Geophysical Journal International 184, 477-493.

Moorkamp, M., Roberts, A.W., Jegen, M., Heincke, B., Hobbs, R.W., 2013. Verification of velocity-resistivity relationships derived from structural joint inversion with borehole data. Geophysical Research Letters 40, 3596-3601.

More, J.J., Thuente, D.J., 1994. Line search algorithms with guaranteed sufficient decrease. ACM Transactions on Mathematical Software 20, 286-307.

Orlando, L., 2013. GPR to constrain ERT data inversion in cavity searching: theoretical and practical applications in archaeology. Journal of Applied Geophysics 89, 35-47.

Pidlisecky, A., Haber, E., Knight, R., 2007. RESINVM3D: A 3D resistivity inversion package. Geophysics 72, H1-H10.

Podvin, P., Lecomte, I., 1991. Finite difference computation of traveltimes in very contrasted velocity models: a massively parallel approach and its associated tools. Geophysical Journal International 105, 271-284.

Shahrukh, M., Soupios, P., Papadopoulos, N., Sarris, A., 2012. Geophysical investigations at the Istron archaeological site, eastern Crete, Greece using seismic refraction and electrical resistivity tomography. Journal of Geophysics and Engineering 9, 749-760.

Shi Z.J., Tian G., Hobbs R.W., Wo H.W., Lin J.X., Wu L.Y., Liu H.Y., 2015, Magnetic gradient and ground penetrating radar prospecting of buried earthen archaeological remains at the Qocho

City Site in Turpan, China. Near Surface Geophysics 13,477-484.

Tarantola, A., 2004. Inverse Problem Theory, 1st edn., SIAM, Philadelphia, PA.

Vermeesch, P.M., Morgan, J.V., Christeson, G.L., Barton, P.J., Surendra, A., 2009. Three-dimensional joint inversion of traveltime and gravity data across the Chicxulub impact crater. Journal of Geophysical Research 114, B02105-B02123.

Zhang, J., Morgan, D.F., 1997. Joint seismic and electrical tomography. EEGS Symposium on Applications of Geophysics to Engineering and Environmental Problems, Environ. and Eng. Geophysics. Soc., Keystone, Colo.

Starting slowness model

Starting resistivity model

Model refine

Model refine

$s(m)$

$\rho(m)$

Seis modeling

$s(m)$

$s(m)$

$\rho(m)$

$\rho(m)$

DC modeling

$t(s(m))$

$p(\rho(m))$

Seis misfit calc.

Seis regularization calc.

Cross-gradient calc.

DC regularization calc.

DC misfit calc.

$\phi_{d,seis}(s(m))$

$\phi_{reg,seis}(s(m))$

$\phi_{cross,s/\rho}$

$\phi_{d,dc}(\rho(m))$

$\phi_{reg,dc}(\rho(m))$

Para trans.

Para trans.

Para trans.

Para trans.

Para trans.

$\phi_{d,seis}(m)$

$\phi_{reg,seis}(m)$

$\phi_{cross,m_s/m_\rho}$

$\phi_{reg,dc}(m)$

$\phi_{d,dc}(m)$

Joint object calc.

$\phi_{jo\,int}(m)$

Model update

m

$\Psi(s(m))$

Para trans.

No

Terminal criteria

No

Para trans.

$\Psi(\rho(m))$

Yes

Inversion model

Fig.1. Flowchart of 3-D cross-gradient joint inversion of seismic refraction and DC resistivity data.

0 m

5 m

10 m

20 m

10 m

0 m   0 m

10 m

20 m

20 m

■ current & potential electrodes
■ potential electrodes
• shots
• receivers
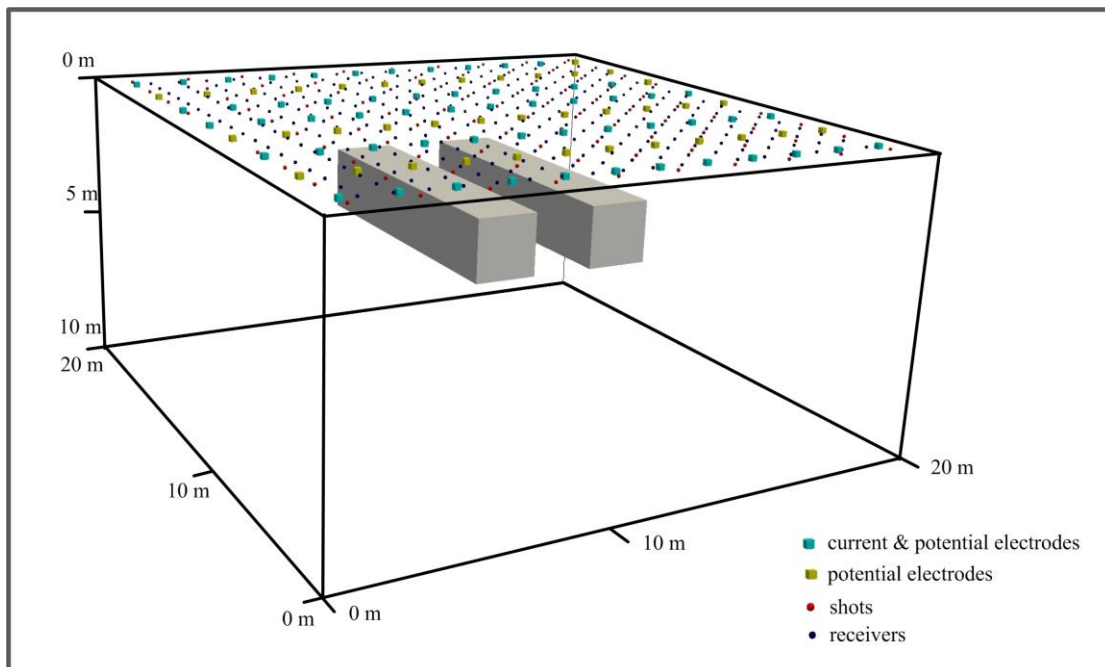
Fig. 2. The synthetic model with two anomalies showing the location of the surface arrays used for computation of the synthetic seismic and resistivity data
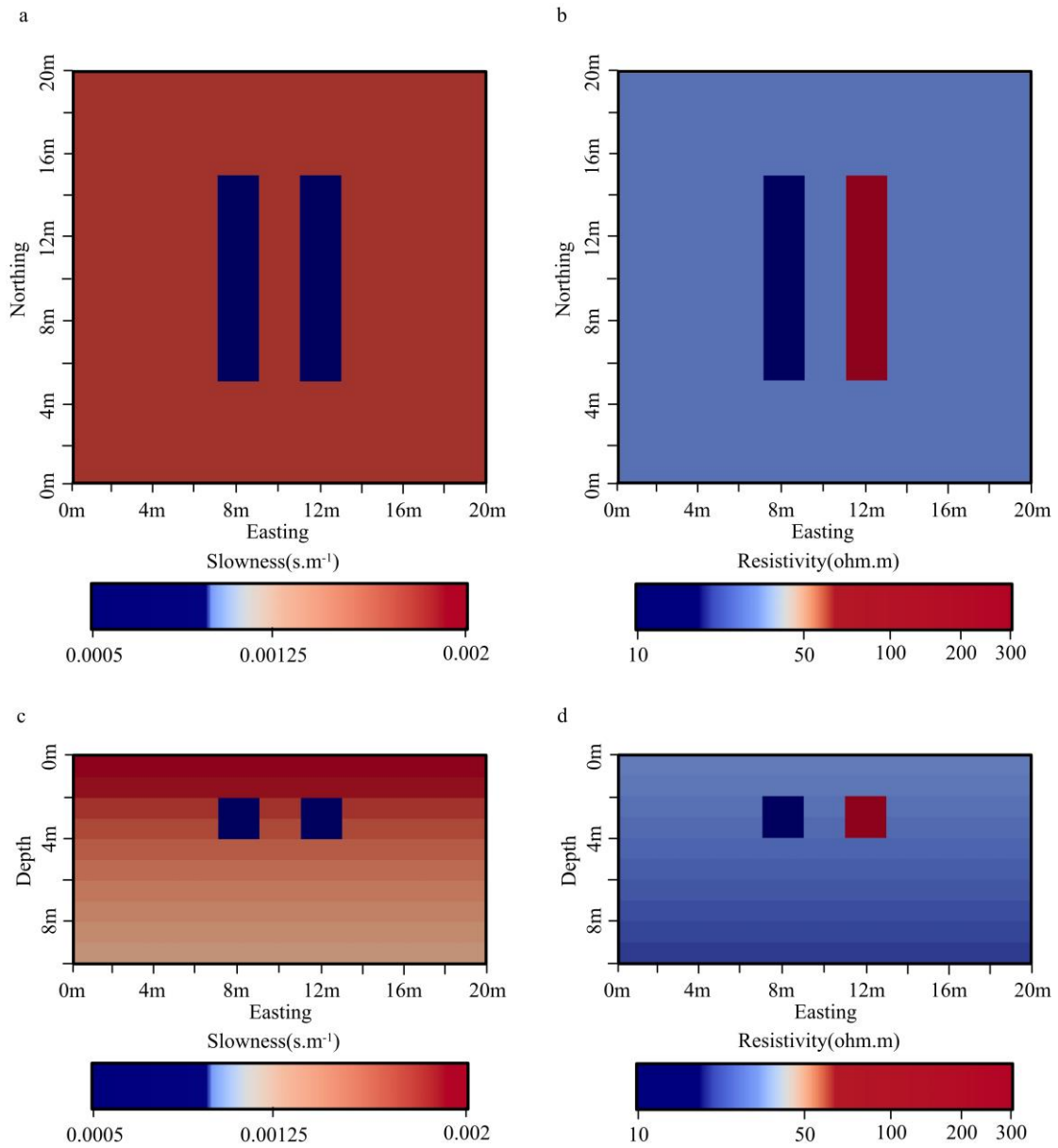
Fig. 3. A plot of true synthetic model. (a) and (b), slowness and resistivity images of horizontal slice at the depth of 3m; (c) and (d), slowness and resistivity images of vertical depth slice through the center of the two anomalies.
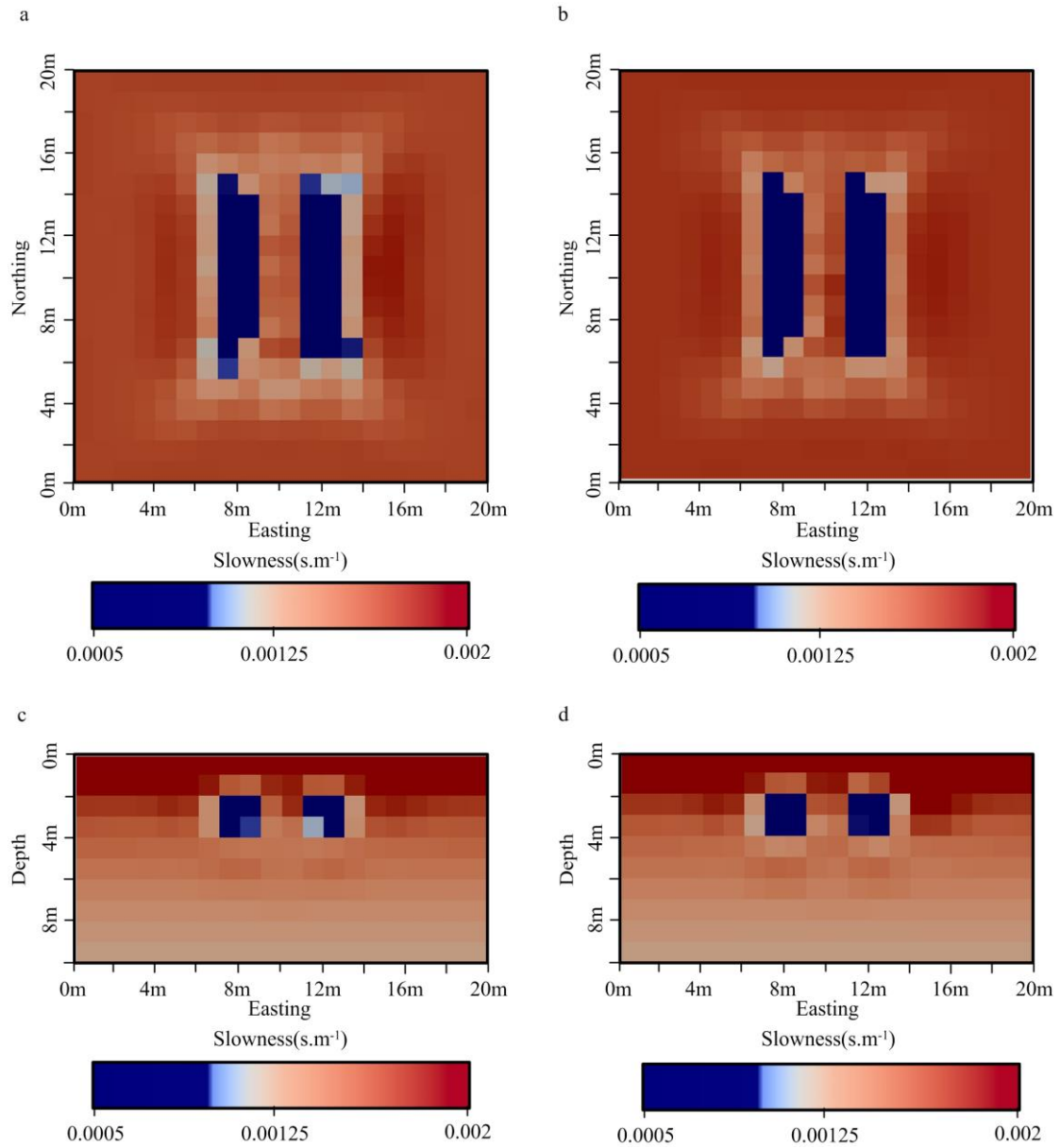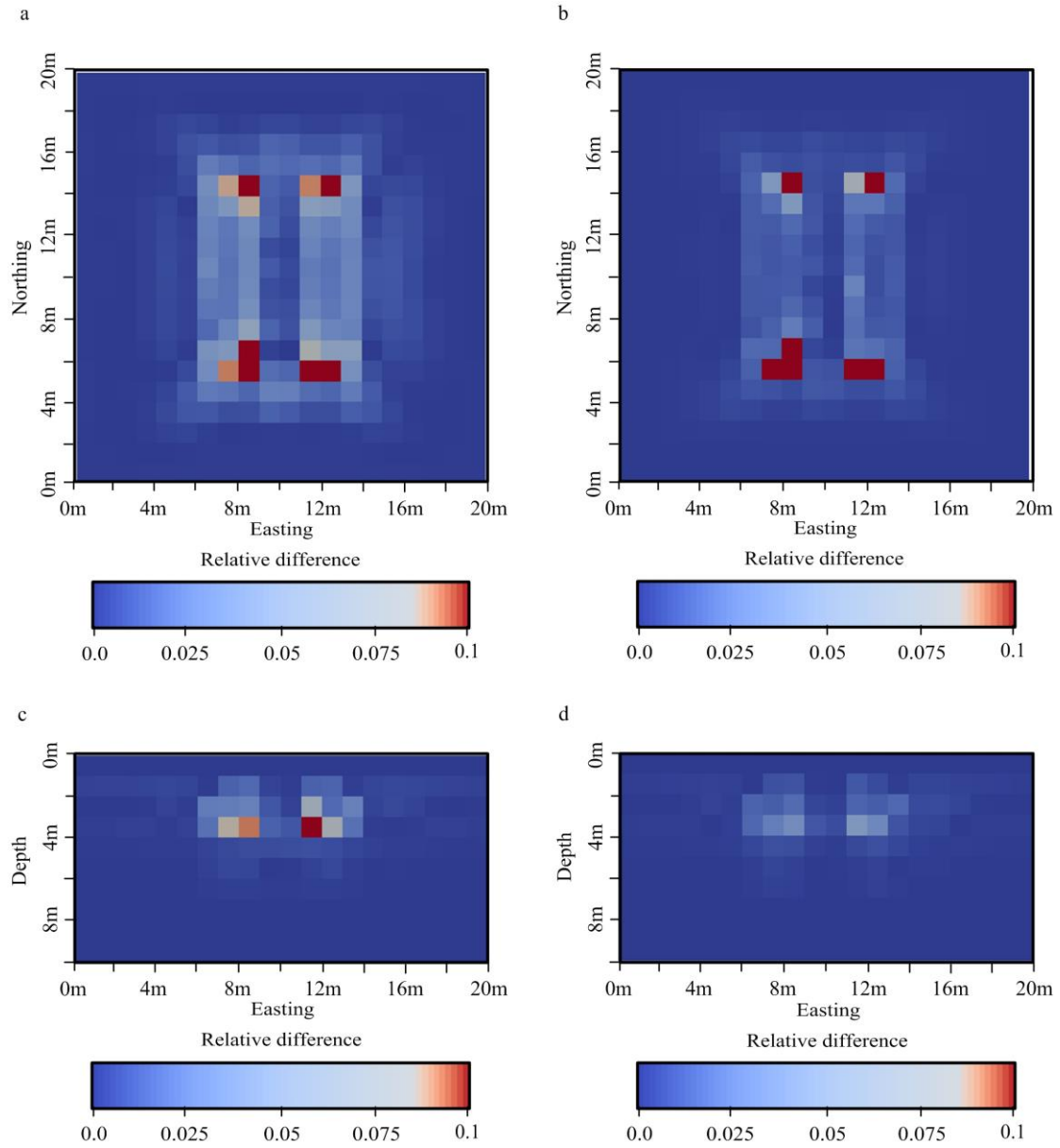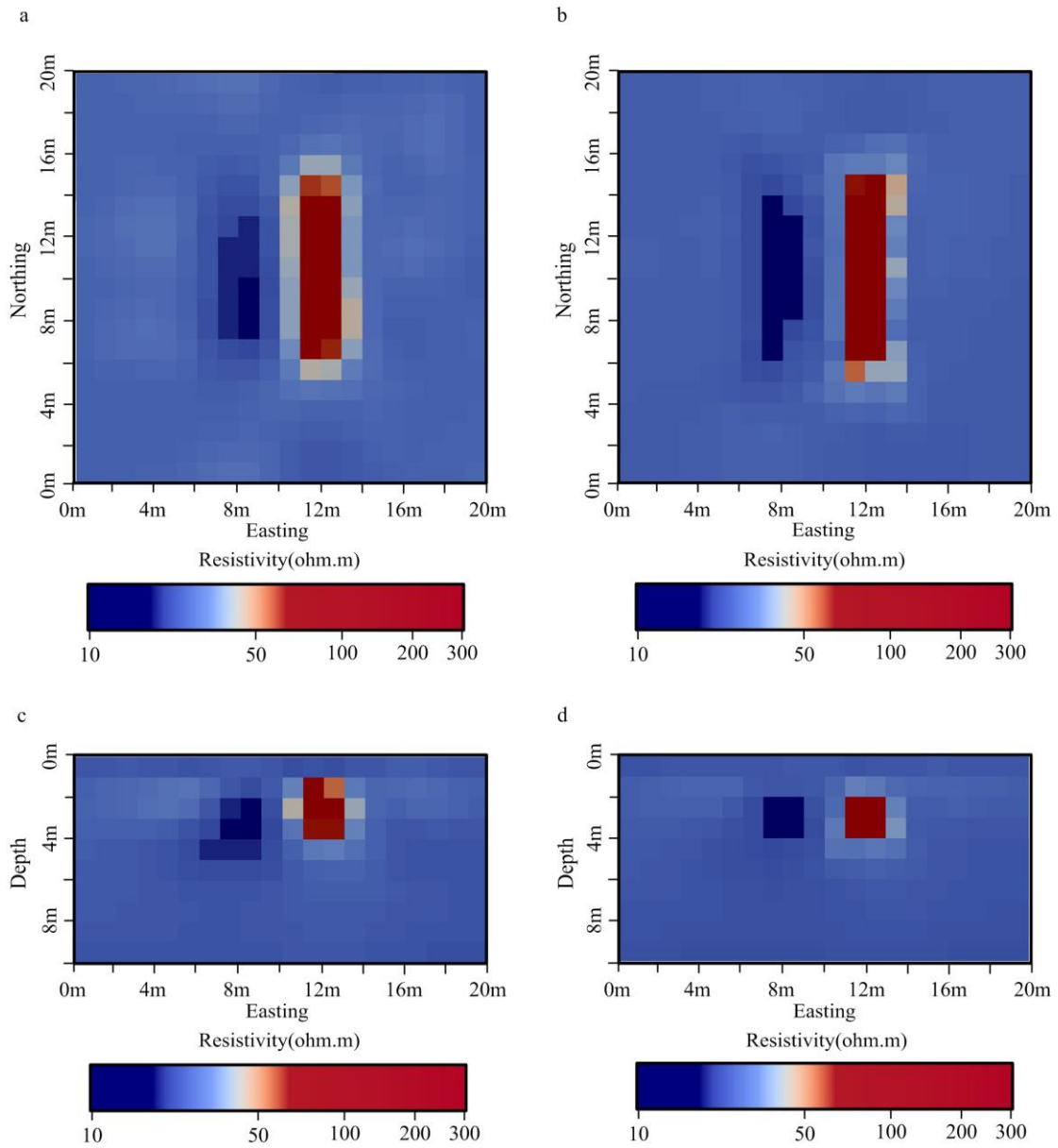
Fig. 4. Results of single inversion and joint inversion for seismic synthetic data without noise. (a) and (b), single inversion and joint inversion slowness images of horizontal slice at the depth of 3m; (c) and (d), single inversion and joint inversion slowness images of vertical depth slice through the center of the two anomalies.
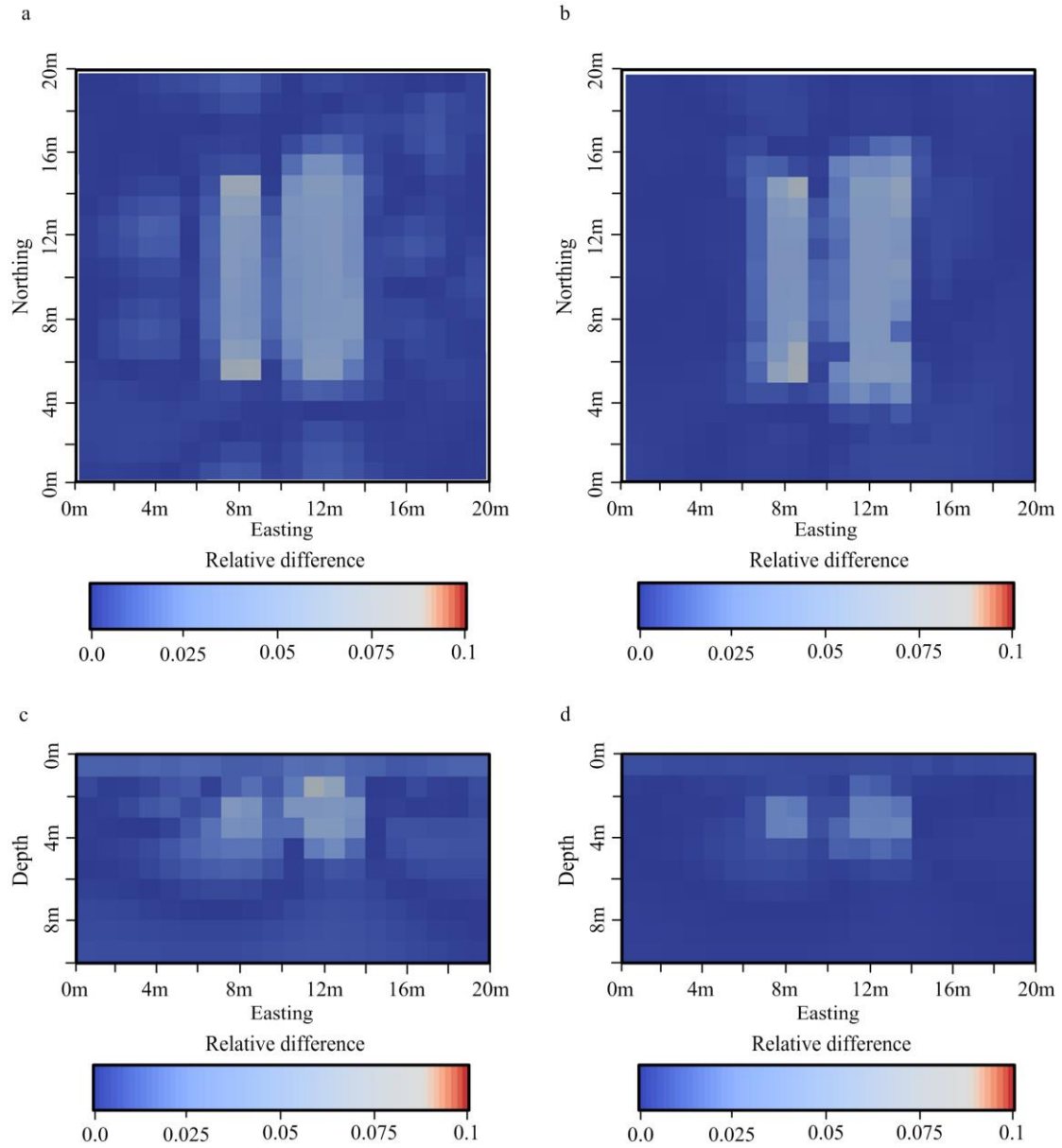
Fig. 5. Relative difference $\left|s^{true} - s^{inv}\right| / s^{true}$ between seismic inversion results shown in Fig. 4 and true model. (a) and (c), horizontal slice at the depth of 3m and vertical depth slice through the model center of relative difference between single inversion result and the true model; (b) and (d), horizontal slice at the depth of 3m and vertical depth slice through the model center of relative difference between joint inversion result and the true model.
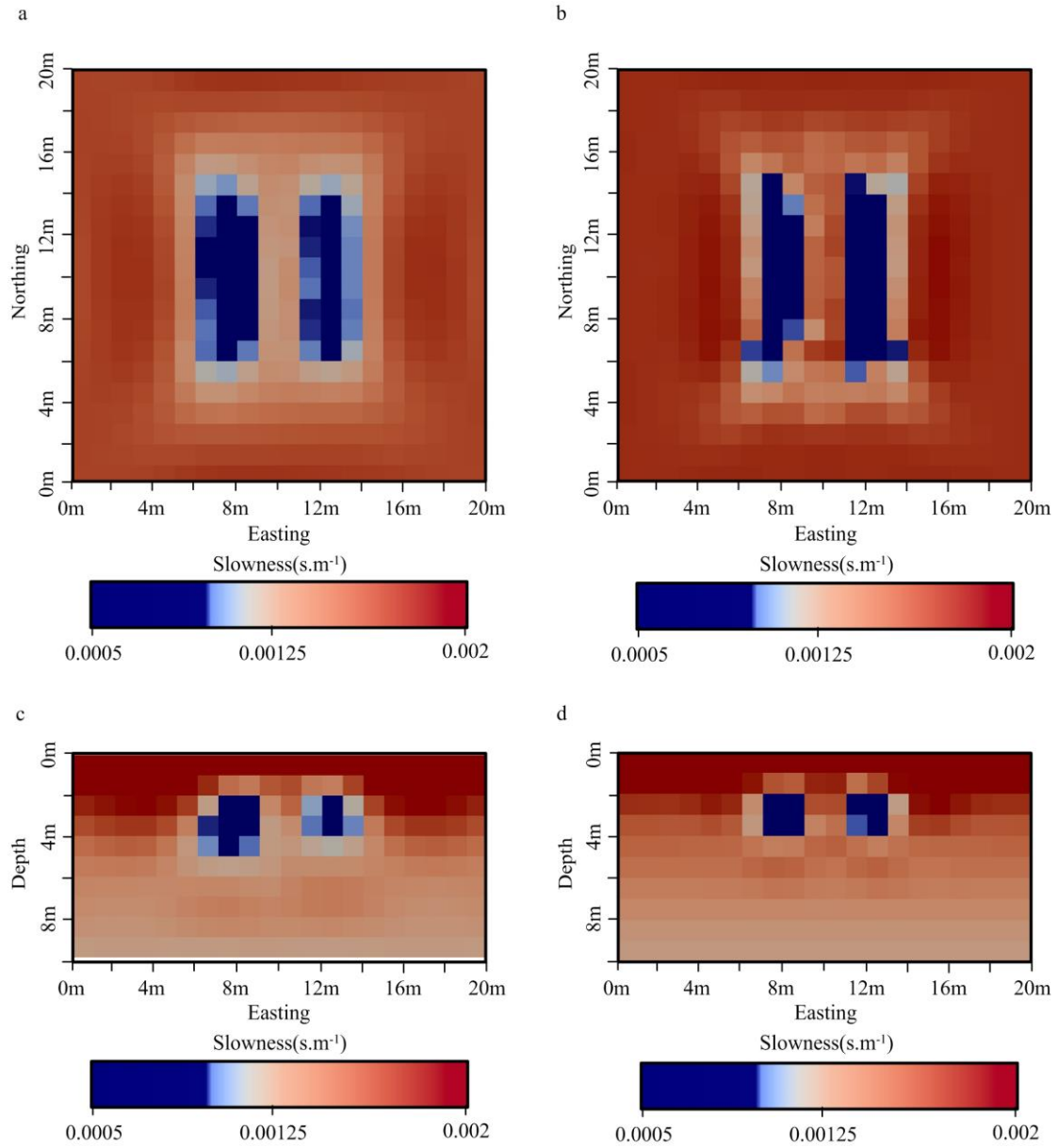
Fig. 6. Results of single inversion and joint inversion for DC resistivity synthetic data without noise. (a) and (b), single inversion and joint inversion resistivity images of horizontal slice at a depth of 3m; (c) and (d), single inversion and joint inversion resistivity images of vertical depth slice through the center of the two anomalies.
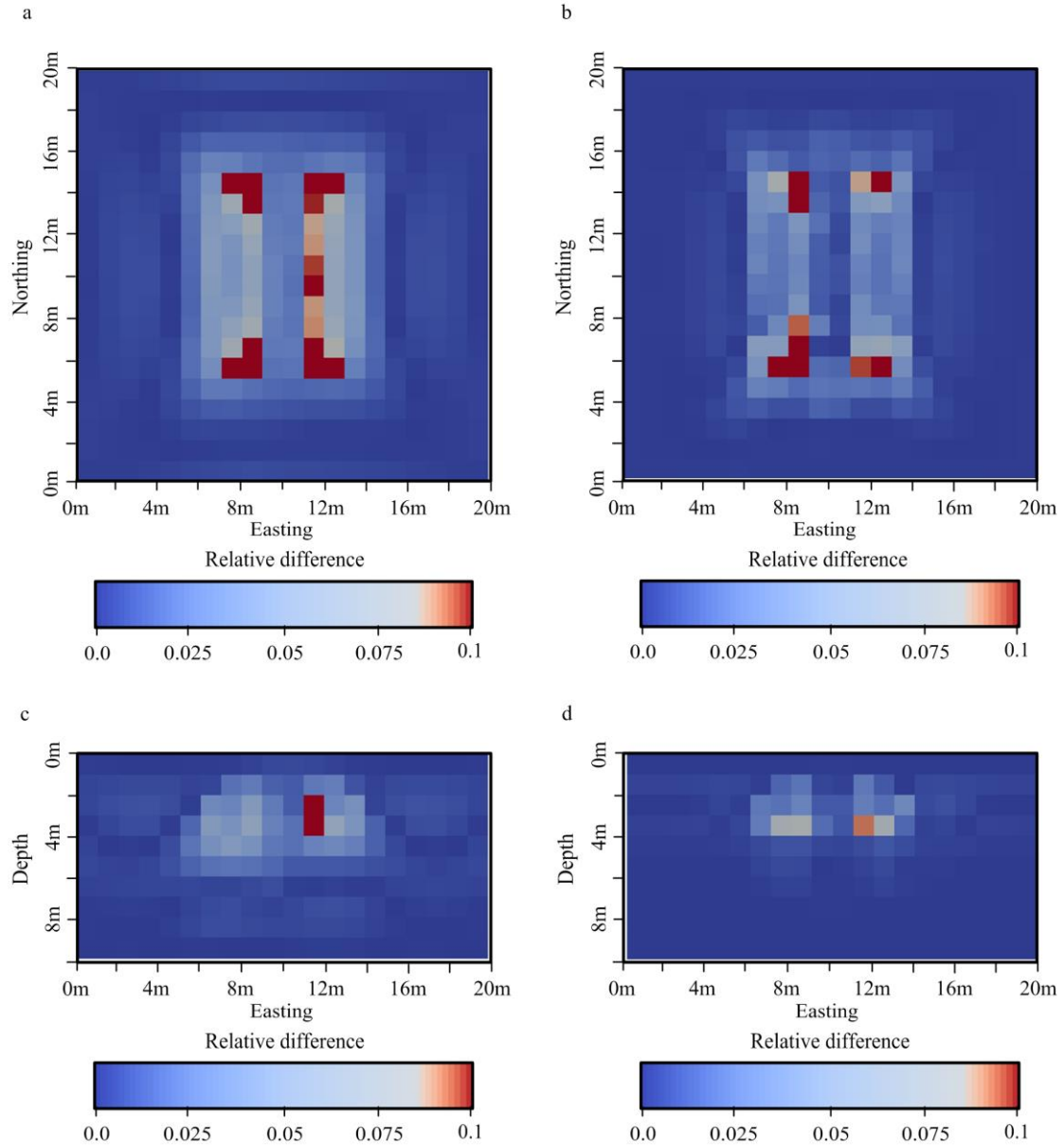
Fig. 7. Relative difference $\left|\rho^{true} - \rho^{inv}\right| / \rho^{true}$ between resistivity inversion results shown in Fig. 6 and true model. (a) and (c), horizontal slice at the depth of 3m and vertical depth slice through the model center of relative difference between single inversion result and the true model; (b) and (d), horizontal slice at the depth of 3m and vertical depth slice through the model center of relative difference between joint inversion result and the true model.
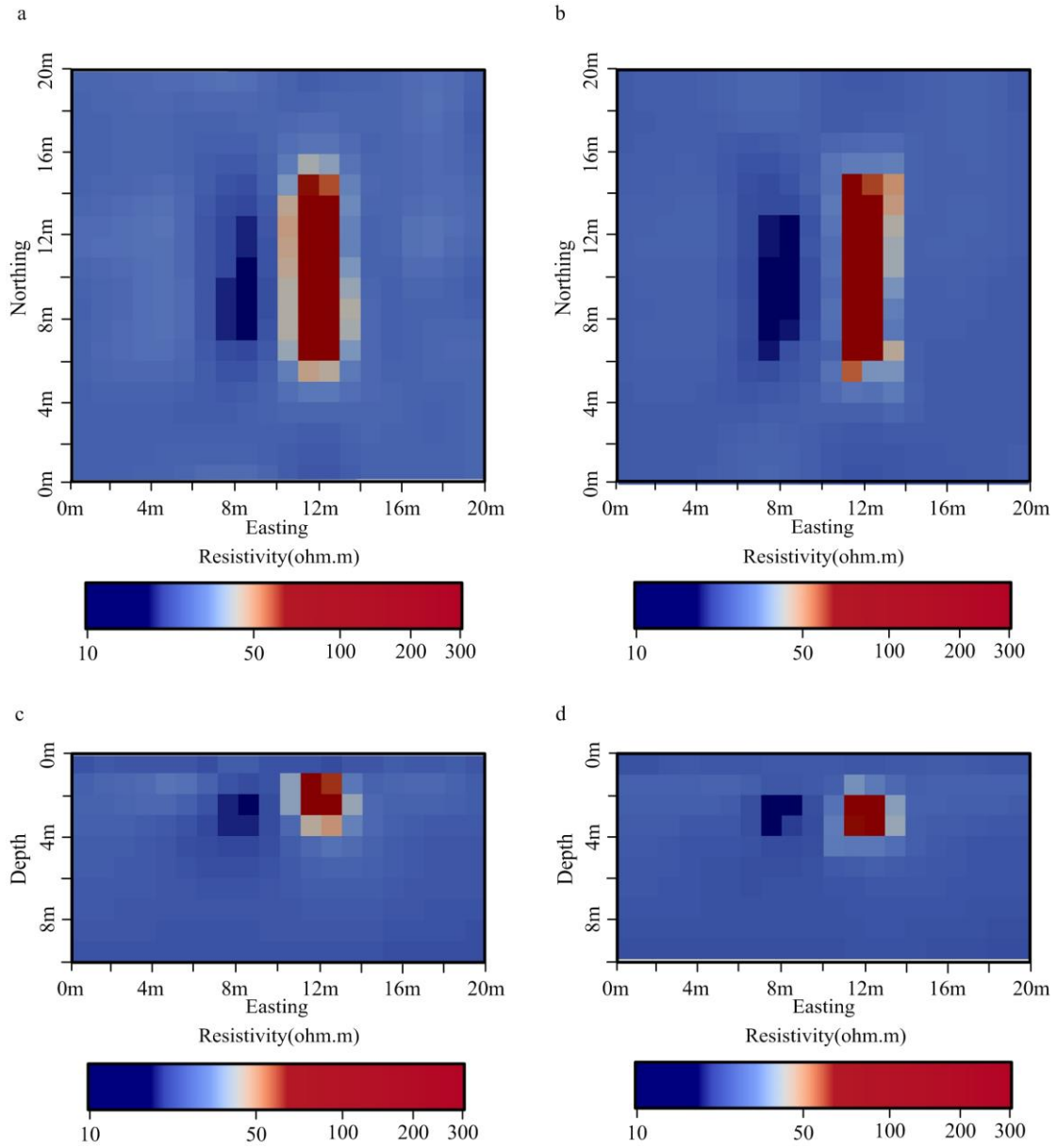
Fig. 8. Results of single inversion and joint inversion for seismic synthetic data with noise. (a) and (b), single inversion and joint inversion slowness images of horizontal slice at a depth of 3m; (c) and (d), single inversion and joint inversion slowness images of vertical depth slice through the center of the two anomalies.

Fig. 9. Relative difference $\left|s^{true}-s^{inv}\right|/s^{true}$ between seismic inversion results shown in Fig. 8 and true model. (a) and (c), horizontal slice at the depth of 3m and vertical depth slice through the model center of relative difference between single inversion result and the true model; (b) and (d), horizontal slice at the depth of 3m and vertical depth slice through the model center of relative difference between joint inversion result and the true model.

Fig. 10. Results of single inversion and joint inversion for DC resistivity synthetic data with noise. (a) and (b), single inversion and joint inversion resistivity images of horizontal slice at a depth of 3m; (c) and (d), single inversion and joint inversion resistivity images of vertical depth slice through the center of the two anomalies.
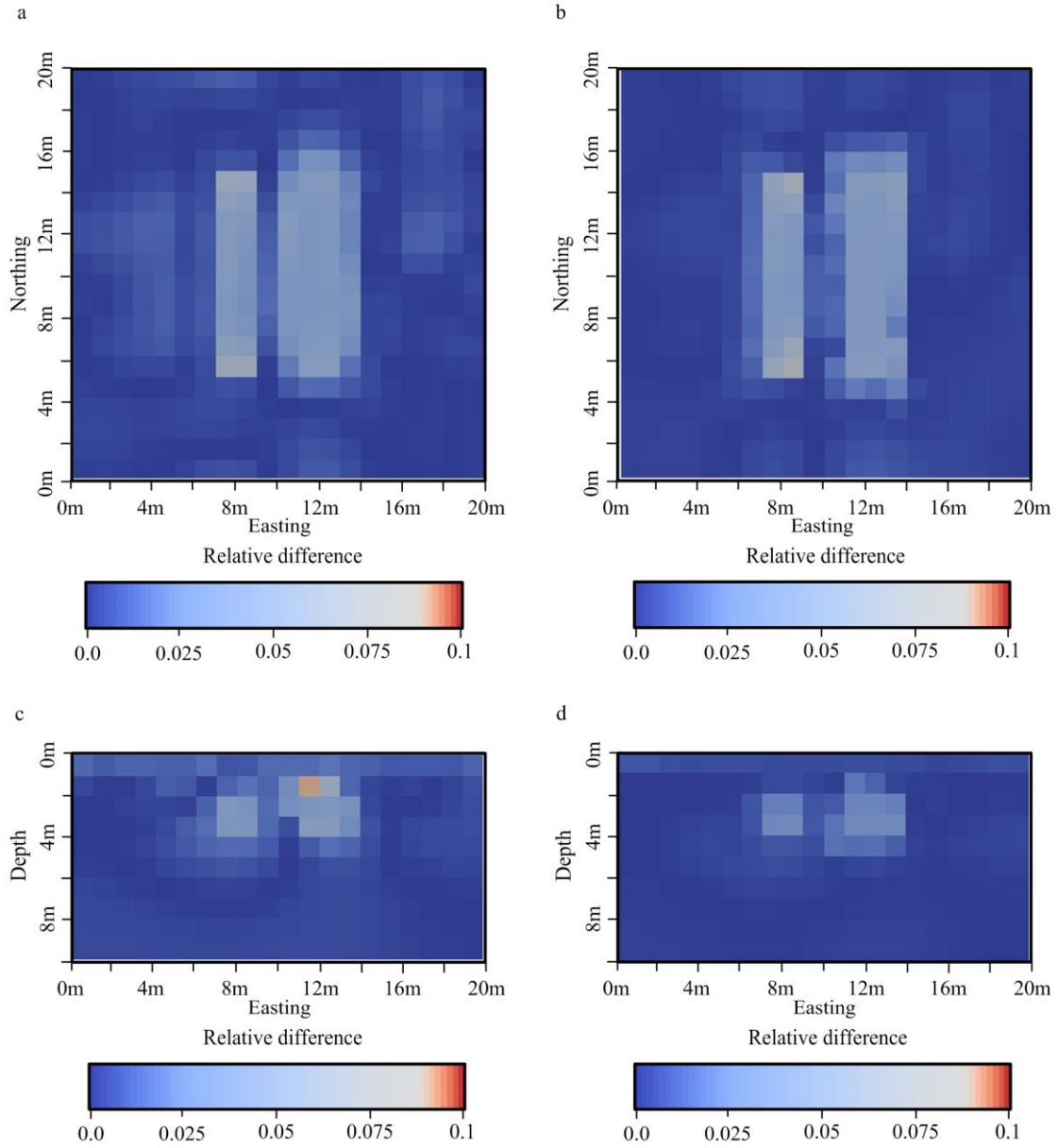
Fig. 11. Relative difference $\left|\rho^{true} - \rho^{inv}\right| / \rho^{true}$ between resistivity inversion results shown in Fig. 10 and true model. (a) and (c), horizontal slice at the depth of 3m and vertical depth slice through the model center of relative di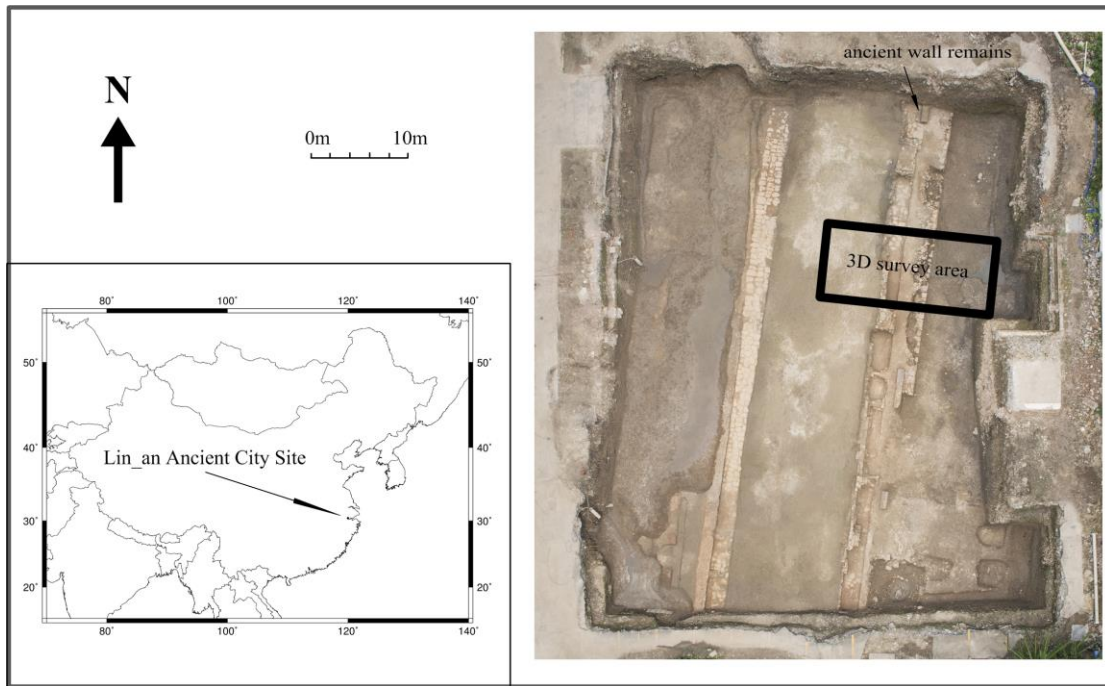fference between single inversion result and the true model; (b) and (d), horizontal slice at the depth of 3m and vertical depth slice through the model center of relative difference between joint inversion result and the true model.

Fig. 12. The position of experiment site in Hangzhou of China, location of 3D survey, and aerial photograph of the area after archaeological excavation.
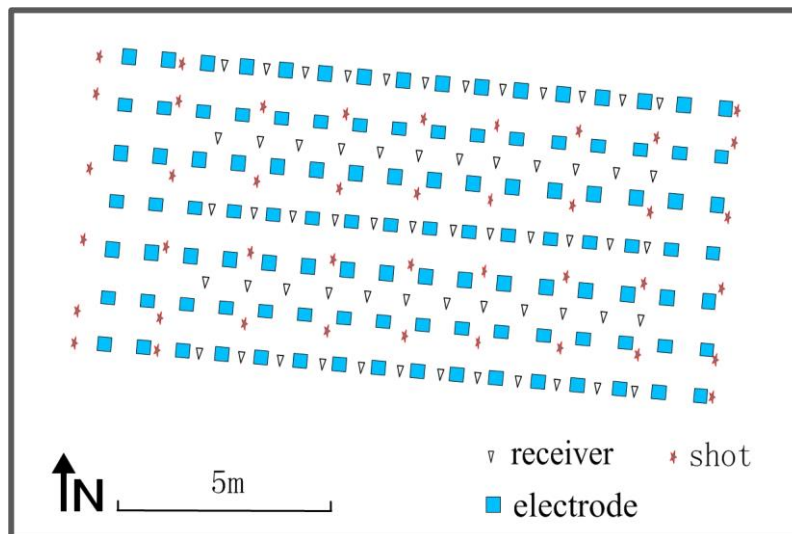

Fig. 13. The relative location of seismic sources, receivers and electrodes for the acquisition of 3D seismic refraction and DC resistivity field data.
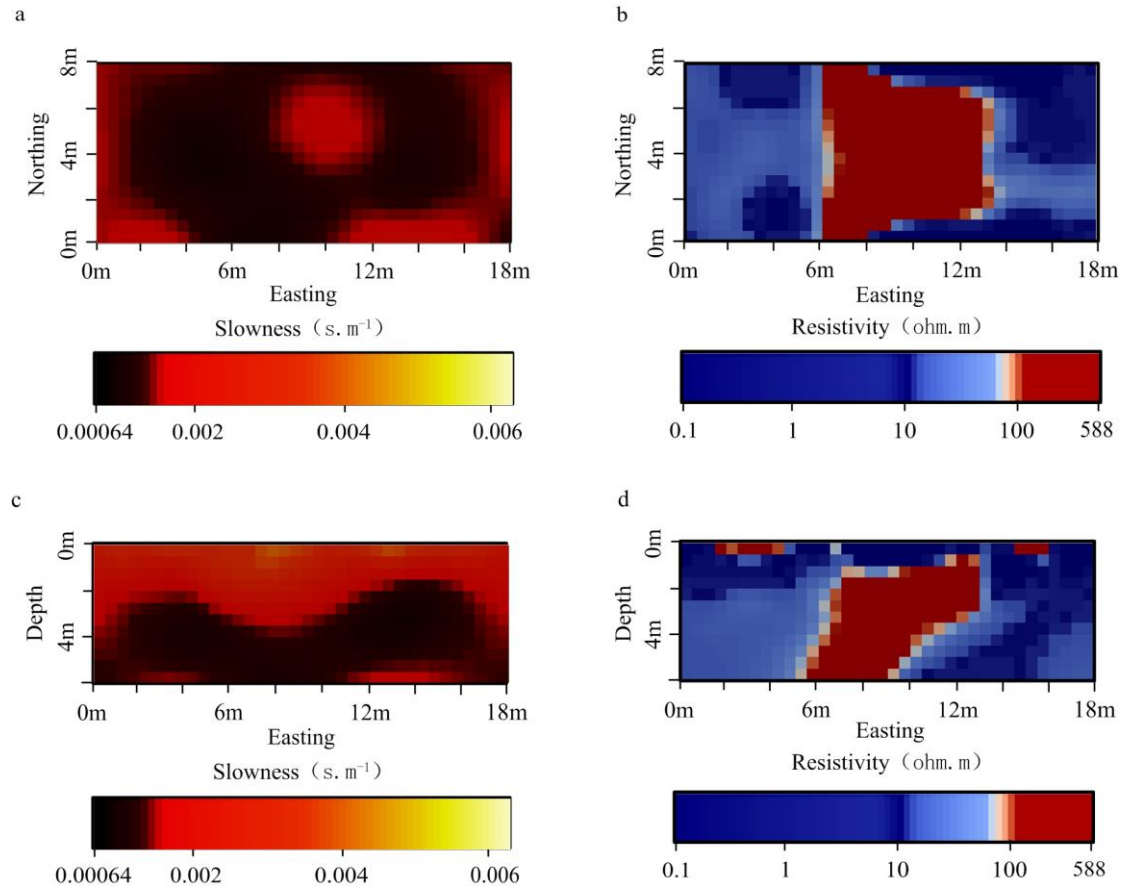
Fig. 14. Results of single inversion for seismic refraction and DC resistivity field data from Lin_an ancient city site. (a) and (b), slowness and resistivity images of horizontal slice at a depth of 3.5m; (c) and (d), slowness and resistivity images of vertical depth slice through the center of the survey area.
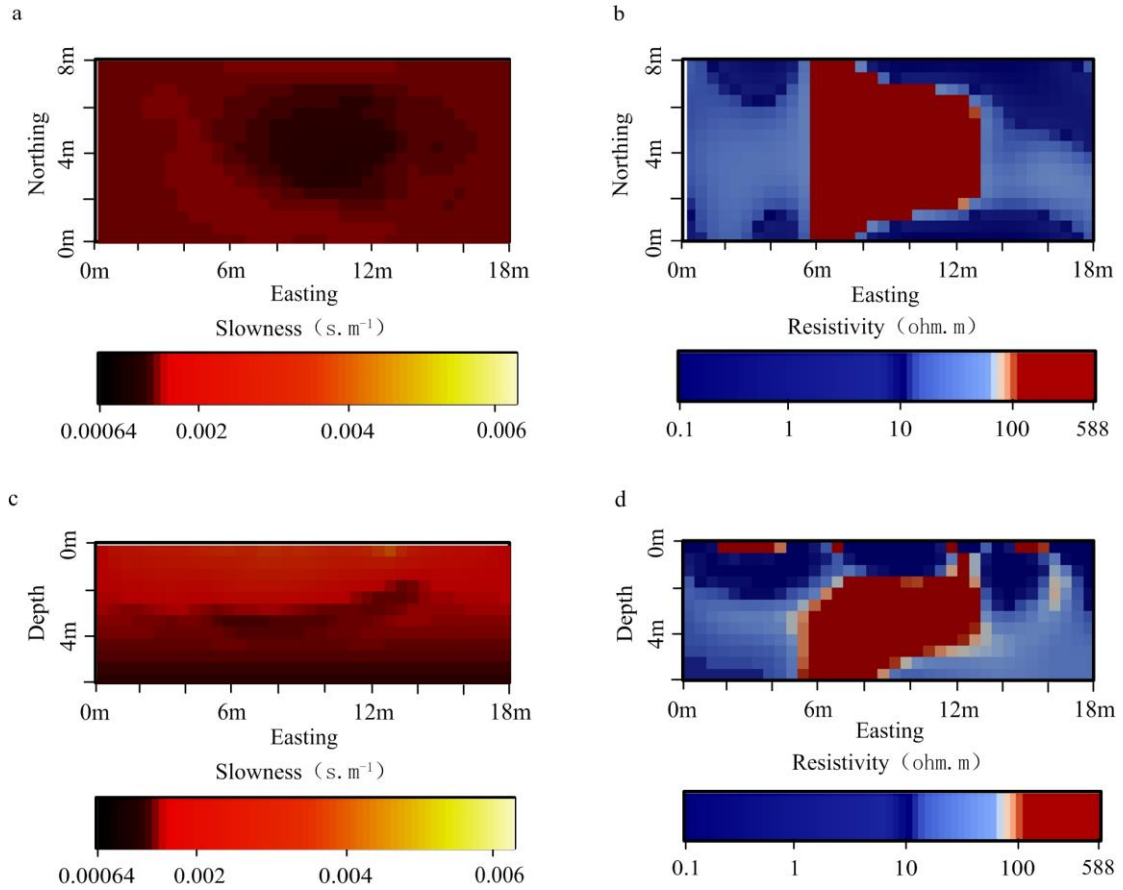
Fig. 15. Results of joint inversion for seismic refraction and DC resistivity field data from Lin_an ancient city site. (a) and (b), slowness and resistivity images of horizontal slice at a depth of 3.5m; (c) and (d), slowness and resistivity images of vertical depth slice through the center of the survey area.